2023 IEEE/ASME International Conference on Advanced Intelligent Mechatronics (AIM)
June 28-30, 2023. Seattle, Washington, USA

Modulation of Joint Stiffness for Controlling the Cartesian Stiffness of a 2-DOF Planar Robotic Arm for Rehabilitation

Thanapol Tantagunninat, Narakorn Wongkaewcharoen, Khemwutta Pornpipatsakul, Rada Chuengpichanwanich, and Ronnapee Chaichaowarat, *Member, IEEE*

Abstract—This paper presents a method for achieving Cartesian stiffness control at the endpoint of a 2-degree-of-freedom planar robotic arm by modulating joint stiffnesses. Planar robotic arms are widely applied for upper-limb rehabilitation through impedance control, but not generally in Cartesian stiffness control through joint stiffness. A modular robotic actuator with integrated controllers on a robot prototype enables the direct command of desired joint stiffness. A closed-form solution was derived through the Jacobian matrix to map the stiffnesses of a reference equilibrium. In addition, the prediction of the joint displacement corresponding to the endpoint motion is required for computing the needed joint stiffnesses. The proposed method is experimentally validated by recording the Cartesian force against the unidirectional displacement at different robotic arm configurations, showing a linear relationship. The results suggest that the proposed method has the potential for use in rehabilitation tasks when the direction of the endpoint displacement is predetermined. The method allows a precise control of the robotic arm's stiffness, which can help in creating more efficient rehabilitation protocols on an easily accessible and affordable rehabilitation robot. Nonetheless, further work is needed to improve the accuracy and omnidirectional robustness of the control method. The study also highlights the importance of designing a robotic arm to satisfy stiffness requirements in addition to kinematic optimization for sufficient workspaces.

I. Introduction

Robot-assisted rehabilitation therapy has been proven to be effective for restoring upper limb motor dysfunction through repetitive trainings [1]–[3]. Robotics offers an opportunity to increase patients' training intensity of motor practice required to "relearn" their lost motor skills while potentially reducing the participation of therapists. Depending on a patient's residual motor capabilities, different robot operation modes, namely, passive, assist-as-needed, or active, are required [4]. The trajectory is fully controlled by the robot if the patient cannot move. If the patient can start a movement but cannot reach a target, the robot helps complete the task. The robot exerts a set of programmed force fields to stimulate the patient to express their attempts to complete the movement from the program. The trajectory depends on the interaction between the robot and the human limb.

T. Tantagunninat and N. Wongkaewcharoen were with the Department of Mechanical Engineering, Chulalongkorn University, Bangkok 10330 Thailand. These authors contributed equally to this work. K. Pornpipatsakul and R. Chuengpichanwanich are with the Department of Mechanical Engineering, Chulalongkorn University, Bangkok 10330 Thailand. R. Chaichaowarat is with the International School of Engineering, Chulalongkorn University, Bangkok 10330 Thailand (e-mail: ronnapee.c@chula.ac.th).

The effectiveness of the end-effector robot intervention over the exoskeleton robot intervention for patients with chronic stroke and moderate-to-severe upper-limb impairment has been reported [5]. For the assist-as-needed training, a controller that constructs a virtual channel along a predetermined training trajectory was proposed [6]. Despite the use of active force feedback, achieving low mechanical impedance is still a major concern in adapting industrial robots for use in rehabilitation. A belt-driven planar Cartesian robot [7] allows low impedance for back-drivability and provides isotropic inertial properties independent of the robot configuration in the workspace. However, further studies on the friction and effects of belts' compliance are required. Most rehabilitation robots are technically advanced and mainly designed for clinical use. An affordable device for upper-limb neurorehabilitation using a 2-degree-of-freedom (DOF) five-bar parallel kinematic mechanism was designed for home use [8]. By applying a tabletop as the plane of motion and supporting the vertical load from the forearm at the endpoint, the compact design of robot arms and bearing supports is acceptable because structural rigidity is not a significant concern.

Direct mechanical coupling always exists between a patient and machine, but their interacting condition can significantly vary. Two complementary strategies are used for the modulation of mechanical impedance for successful physical human–robot interactions: the first is feedback control [9]–[11] and the second is adjusting the intrinsic properties of actuators [12] [13]. Controlling the Cartesian stiffness on the plane of motion is important for upper-extremity planar rehabilitation robots. The Cartesian impedance control was proposed for a variable-stiffness robot arm, where the active impedance controller was implemented in combination with passive joints to increase the achievable range of stiffness [14]. The performance of the impedance controller was enhanced by taking advantage of the fast joint control loop [15]. Using a brushless DC hobby motor and accurate encoder, the modular actuator with an integrated controller and planetary gear reduction [16] was introduced for dynamic robots. The motors allow the convenient control of the joint stiffness and position.

Although many planar rehabilitation robot studies have been conducted, methods for achieving the desired planar stiffness by controlling the joint stiffness are not widely used. Accordingly, this paper proposes an alternative strategy to achieve the desired Cartesian stiffness at the endpoint through the individual joint stiffness control using an integrated controller for affordable modular robotic actuators. We present our built prototype of a 2-DOF serial manipulator for upper-extremity rehabilitation, aiming to make

978-1-6654-7633-1/23/$31.00 ©2023 IEEE

rehabilitation robots portable, affordable, and easily accessible.

This paper is organized as follows: Section II derives a closed-form solution for calculating joint stiffnesses to satisfy a desired Cartesian stiffness. Section III discusses the region-dependent stiffness controllability through simulation results. Section IV describes the hardware and experimental setup. Section V discusses the experimental validation results. Finally, Section VI summarizes the key findings.

II. Derivation of Joint Stiffnesses from a Desired Cartesian Stiffness

A. Kinematics of a 2-DOF Planar Robotic Arm

Robot kinematics is necessary for calculating the relationship between the joint and Cartesian displacements. Figure 1(a) shows a 3D model of the 2-DOF planar robotic arm prototype. The system is actuated by two concentric motors installed on an aluminum extrusion frame. The first link is directly driven by the first motor, whereas the second link is driven by the second motor through the input link and coupler of the four-bar linkage mechanism. To derive the robot kinematics, the configuration of the robot arm is shown in Fig. 1(b). The origin of the X–Y plane is located at the center of both motors. The lengths of l_1 and l_2 are 275 and 240 mm, respectively. The joint displacements θ_1 measured from the X-axis and θ_2 measured from the Y-axis are positive in the clockwise direction. The origin position of the robot is defined at $\theta_1 = \theta_2 = 0°$. When the first link points along the X-axis, the offset angle between the input link and negative Y-axis is $\theta_0 = 18°$.

The kinematic equations relating the end-effector Cartesian position (x, y) to the joint angles (θ_1, θ_2) are given by (1)–(2).

$$x = l_1 \cos\theta_1 - l_2 \sin\theta_2 \tag{1}$$

$$y = l_1 \sin\theta_1 + l_2 \cos\theta_2 \tag{2}$$

Considering infinitesimal displacements, the relationship between the Cartesian displacement ($[dx \quad dy]^T$) and angular displacements ($[d\theta_1 \quad d\theta_2]^T$) through the Jacobian matrix is given by (3)–(4).

$$\begin{bmatrix} dx \\ dy \end{bmatrix} = J \begin{bmatrix} d\theta_1 \\ d\theta_2 \end{bmatrix} \tag{3}$$

$$J = \begin{bmatrix} \frac{\partial x}{\partial \theta_1} & \frac{\partial x}{\partial \theta_2} \\ \frac{\partial y}{\partial \theta_1} & \frac{\partial y}{\partial \theta_2} \end{bmatrix} = \begin{bmatrix} -l_1 \sin\theta_1 & -l_2 \cos\theta_2 \\ l_1 \cos\theta_1 & -l_2 \sin\theta_2 \end{bmatrix} \tag{4}$$

B. Achieving a Desired Cartesian Stiffness by Joint Stiffness

The planar robotic arm is rigidly attached to actuators at the origin, so a relationship between the Cartesian stiffness and joint stiffness should be determined. First, we assume that the reaction force at the endpoint along the X-axis and Y-axis $\left(F_x, F_y\right)$ is generated from a linear spring with the desired stiffnesses k_x and k_y (see (5)).

$$\begin{bmatrix} \mathrm{F_x} \\ \mathrm{F_y} \end{bmatrix} = \begin{bmatrix} \mathrm{k_x}\bar{\mathrm{x}} \\ \mathrm{k_y}\bar{\mathrm{y}} \end{bmatrix} \tag{5}$$

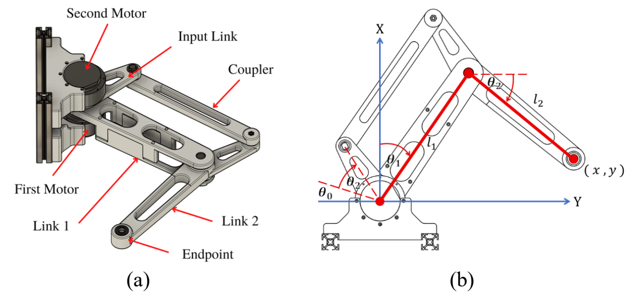

Fig. 1. (a) CAD rendering model showing the components of the robotic arms. (b) Top-view diagram shows the configuration of the robotic arm.

The spring deformation $[\bar{x} \quad \bar{y}]^T$ defined by (6) is the distance between the endpoint $[x \quad y]^T$ and reference point $[x_0 \quad y_0]^T$.

$$\begin{bmatrix} \bar{x} \\ \bar{y} \end{bmatrix} = \begin{bmatrix} x - x_0 \\ y - y_0 \end{bmatrix} \tag{6}$$

The equivalent torques of motors $[\tau_1 \quad \tau_2]^T$ can be determined from the Cartesian forces at the endpoint, as given by (7).

$$\begin{bmatrix} \tau_1 \\ \tau_2 \end{bmatrix} = J^T \begin{bmatrix} F_x \\ F_y \end{bmatrix} \tag{7}$$

Through the substitution of $\bar{x}$ and $\bar{y}$ from (6) into (5), the corresponding joint torques are computed via (7), as (8).

$$\begin{bmatrix} \tau_1 \\ \tau_2 \end{bmatrix} = \begin{bmatrix} k_x \bar{x} \frac{\partial x}{\partial \theta_1} + k_y \bar{y} \frac{\partial y}{\partial \theta_1} \\ k_x \bar{x} \frac{\partial x}{\partial \theta_2} + k_y \bar{y} \frac{\partial y}{\partial \theta_2} \end{bmatrix} \tag{8}$$

In (9), the components of the torsional stiffness matrix K_q can be obtained by solving the partial differential equation of the corresponding torque with the angular displacements (θ_1, θ_2).

$$K_q = \begin{bmatrix} k_{q11} & k_{q12} \\ k_{q21} & k_{q22} \end{bmatrix} \tag{9}$$

$$k_{q11} = k_x \left[\left(\frac{\partial x}{\partial \theta_1} \right)^2 + \bar{x} \frac{\partial^2 x}{\partial \theta_1^2} \right] + k_y \left[\left(\frac{\partial y}{\partial \theta_1} \right)^2 + \bar{y} \frac{\partial^2 y}{\partial \theta_1^2} \right]$$

$$k_{q12} = k_x \left[\left(\frac{\partial x}{\partial \theta_1} \right) \left(\frac{\partial x}{\partial \theta_2} \right) + \bar{x} \frac{\partial^2 x}{\partial \theta_2 \partial \theta_1} \right] + k_y \left[\left(\frac{\partial y}{\partial \theta_1} \right) \left(\frac{\partial y}{\partial \theta_2} \right) + \bar{y} \frac{\partial^2 y}{\partial \theta_2 \partial \theta_1} \right]$$

$$k_{q21} = k_x \left[\left(\frac{\partial x}{\partial \theta_1} \right) \left(\frac{\partial x}{\partial \theta_2} \right) + \bar{x} \frac{\partial^2 x}{\partial \theta_1 \partial \theta_2} \right] + k_y \left[\left(\frac{\partial y}{\partial \theta_1} \right) \left(\frac{\partial y}{\partial \theta_2} \right) + \bar{y} \frac{\partial^2 y}{\partial \theta_1 \partial \theta_2} \right]$$

$$k_{q22} = k_x \left[\left(\frac{\partial x}{\partial \theta_2} \right)^2 + \bar{x} \frac{\partial^2 x}{\partial \theta_2^2} \right] + k_y \left[\left(\frac{\partial y}{\partial \theta_2} \right)^2 + \bar{y} \frac{\partial^2 y}{\partial \theta_2^2} \right]$$

where $\frac{\partial^2 x}{\partial \theta_1 \partial \theta_2} = \frac{\partial^2 x}{\partial \theta_2 \partial \theta_1} = \frac{\partial^2 y}{\partial \theta_1 \partial \theta_2} = \frac{\partial^2 y}{\partial \theta_2 \partial \theta_1}$.

With a predicted displacement in the Cartesian space, the torque is determined by (10), where $k_{\theta 1}$ and $k_{\theta 2}$ are the joint angular stiffnesses and $[\Delta\theta_1 \quad \Delta\theta_2]^T$ is the angular distance between the specified angle ($[\theta_1 \quad \theta_2]^T$) and its initial position.

$$\tau = \begin{bmatrix} k_{\theta 1} & 0 \\ 0 & k_{\theta 2} \end{bmatrix} \begin{bmatrix} \Delta\theta_1 \\ \Delta\theta_2 \end{bmatrix} = \begin{bmatrix} \mathrm{k_{q11}} & \mathrm{k_{q12}} \\ \mathrm{k_{q21}} & \mathrm{k_{q22}} \end{bmatrix} \begin{bmatrix} \Delta\theta_1 \\ \Delta\theta_2 \end{bmatrix} \tag{10}$$

Accordingly, the joint stiffnesses required by the actuators are described in (11) and (12).

$$k_{\theta 1} = k_{q11} + \frac{\Delta\theta_2}{\Delta\theta_1} k_{q12} \tag{11}$$

$$k_{\theta 2} = k_{q22} + \frac{\Delta\theta_1}{\Delta\theta_2} k_{q21} \tag{12}$$

In particular, the joint stiffness of each actuator only depends on k_x (or k_y) when the endpoint purely moves along the X (or Y) direction because $\bar{y}$ (or $\bar{x}$) in (6) is zero.

III. Region-Dependent Stiffness Controllability

In this section, the derived closed-form solution is used to simulate the joint stiffnesses $k_{\theta 1}$ and $k_{\theta 2}$ around the workspace covering the joints' limit. The ratio of the joint stiffness over the Cartesian stiffness is computed for the conditions when the endpoint purely moves for 30 mm along the Y-axis $[\bar{x} \quad \bar{y}]^T=[0 \quad 0.03]^T$ and when the endpoint purely moves for 30 mm along the x-axis $[\bar{x} \quad \bar{y}]^T=[0.03 \quad 0]^T$.

Figure 2 shows the simulated ratio of the joint stiffness $k_{\theta 1}$ over to Cartesian stiffness k_x when the endpoint is moved along the X direction. For any joint angle θ_2, the ratio increases with the joint angle θ_1. The ratio notably increases when the joint angle θ_2 approaches zero. Meanwhile, the ratio of the joint stiffness $k_{\theta 2}$ over the Cartesian stiffness k_x increases with the decrease in the joint angle θ_2 (see Fig. 3). The ratio notably increases when the joint angle θ_1 approaches 90°. Figure 4 shows the simulated ratio of the joint stiffness $k_{\theta 1}$ over to the Cartesian stiffness k_y when the endpoint is moved along the Y direction. For any joint angle θ_2, the ratio increases with the decrease in the joint angle θ_1. The ratio notably increases when the joint angle θ_2 approaches 90°. Meanwhile, the ratio of the joint stiffness $k_{\theta 2}$ over the Cartesian stiffness k_y decreases with the increasing joint angle θ_2 (see Fig. 5). The ratio notably increases when the joint angle θ_2 approaches zero.

As a result, the joint angle of (θ_1, θ_2) = (0, 0)° will be used for experimental validation as it is the most independent position where the stiffness k_x mainly depends on $k_{\theta 1}$ and k_y mainly depends on $k_{\theta 2}$. The other joint angle combination that will be used is (θ_1, θ_2) = (30, 30)° as it is in the middle of the robot's workspace. Moreover, it is the region that will not result in too much stiffness and torque, which could damage the structure and induce errors in the motor control and measured value.

IV. Stiffness Validation Experiment

A. System Overview of the Experimental Platform

Figure 6 shows the experimental setting for validating the reaction force varying against the displacement at different Cartesian stiffnesses. The prototype of a 2-DOF planar robot using a four-bar linkage mechanism is driven by two modular Robotic actuators (T-Motor AK70-10) with an integrated planetary gearbox and integrated controller enable position and stiffness control. The endpoint of the robot prototype is connected to a six-axis force/torque sensor (ATI Gamma FT06147) via a vertical pin-bearing support, which constrains the relative position between the endpoint and F/T sensor while allowing free rotations. The bottom of the force/torque sensor is mounted on a ball screw's linear carrier, which is actuated by a DC stepper motor (17HS3401).

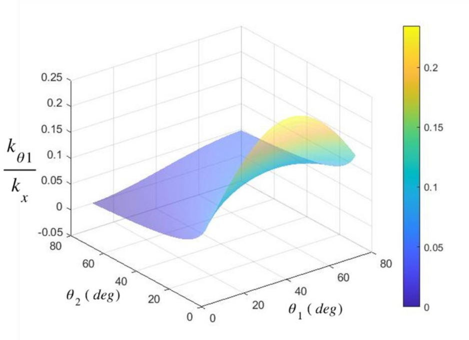

Fig. 2. Ratio of the joint stiffness $k_{\theta 1}$ to the Cartesian stiffness k_x simulated when the endpoint is purely moved along the x-axis direction.

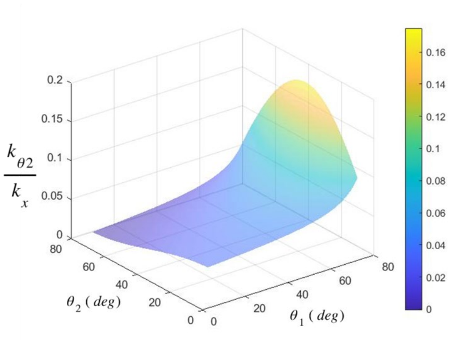

Fig. 3. Ratio of the joint stiffness $k_{\theta 2}$ to the Cartesian stiffness k_x simulated when the endpoint is purely moved along the x-axis direction.

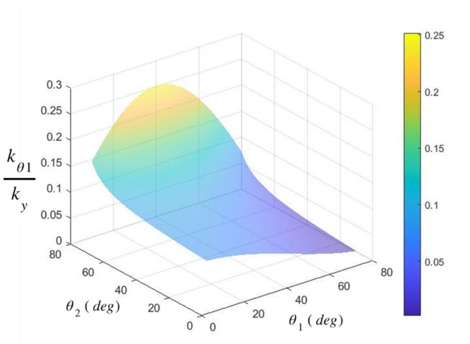

Fig. 4. Ratio of the joint stiffness $k_{\theta 1}$ to the Cartesian stiffness k_y is simulated when the endpoint is purely moved along the x-axis direction.

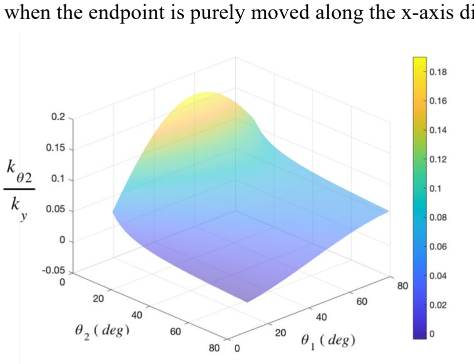

Fig. 5. Ratio of the joint stiffness $k_{\theta 2}$ to the Cartesian stiffness k_y is simulated when the endpoint is purely moved along the x-axis direction.

The experiment was designed to record data at 0° and 30° of each link's angle (θ_1, θ_2). The force/torque sensor was moved along the X- and Y-axes where the linear stiffnesses of the primary testing axis are 500, 1000, 1500, 2000, 2500, and 3000 N/m. The stiffness parameters for each test are

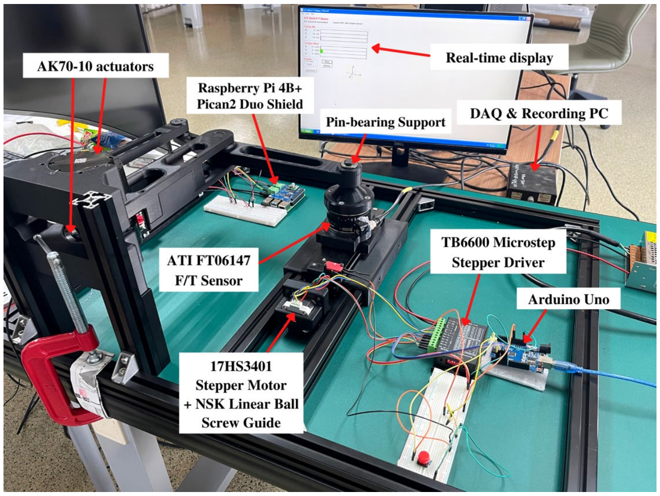

Fig. 6. Experimental setup consisting of two T-Motor AK70-10 actuators, ATI Gamma force/torque sensor, DAQ, PC, ball screw linear actuator, stepper motor, Microstep driver, RaspberryPi microcomputer, CAN-BUS shield, and Arduino Uno microcontroller.

shown in Table I. The reaction force was measured by the F/T sensor at each stop between the linear displacements of −30 mm to 30 mm with a step of 2 mm and operated three cycles per stiffness setting, which will later be averaged.

TABLE I. Stiffness parameters for each test.

$\theta_1 = 0^\circ$, $\theta_2 = 0^\circ$		$\theta_1 = 0^\circ$, $\theta_2 = 0^\circ$		$\theta_1 = 30^\circ$, $\theta_2 = 30^\circ$		$\theta_1 = 30^\circ$, $\theta_2 = 30^\circ$	
Test	kx (N/m)	Test	ky (N/m)	Test	kx (N/m)	Test	ky (N/m)
1	500	7	500	13	500	19	500
2	1000	8	1000	14	1000	20	1000
3	1500	9	1500	15	1500	21	1500
4	2000	10	2000	16	2000	22	2000
5	2500	11	2500	17	2500	23	2500
6	3000	12	3000	18	3000	24	3000

B. Hardware Configuration

To control their stiffnesses, the actuators were controlled by Raspberry Pi 4B with PiCAN2 Duo CAN-Bus shield via CAN communication. The motors received the desired torsional stiffnesses of each motor from the Raspberry Pi. The motor position was set to zero at the testing position. The force/torque sensor was moved by a ball screw carrier, and the stepper motor was controlled by a TB6600 Microstep driver and Arduino UNO, as shown in Fig. 7. The block diagram showing the signal flow from the desired stiffnesses to the reaction forces is displayed in Fig. 8.

V. Experimental Results and Discussion

A. Cartesian Stiffness of Reference Equilibrium Points

At different arm configurations, the Cartesian stiffnesses in the forward–backward direction (Y) and left–right direction (X) were studied in static conditions. At the first equilibrium point, joint angles θ_1 and θ_2 were set to 0°. The two links of the robot arm are perpendicular in this configuration. The forward–backward motion of the endpoint mainly affects the rotation of the first joint, whereas the left–right motion mainly affects the rotation of the second joint. In each direction, the desired Cartesian stiffness varied from 500 to 3,000 N/m. The joint stiffnesses, computed via (11) and (12) using the 30-mm positive displacement, i.e., the

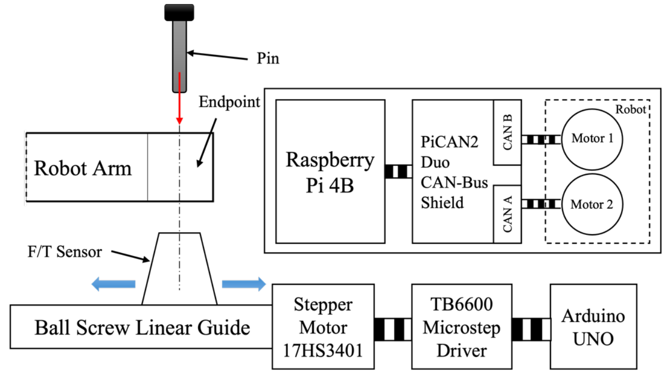

Fig. 7. Diagram showing the experimental hardware. A Raspberry Pi microcomputer was used to control the robot actuators via the CAN-Bus shield. The pin-bearing support connects the robot arm's endpoint and force/torque sensor. The stepper motor is controlled to move the sensor along the linear actuator for testing in different X–Y positions.

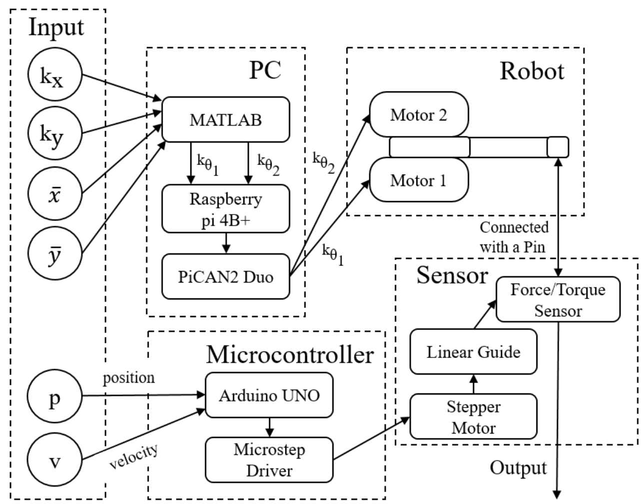

Fig. 8. Diagram showing the signal flow from the angular stiffnesses and the desired position input of the robot actuators and the position and velocity input of the linear actuator to the reaction forces measured at the endpoint for the designated Cartesian positions.

backward motion (+Y direction) or rightward motion (+X direction), were commanded to the motors driving the joints. For each set of constant joint stiffnesses, the linear motor started moving from the equilibrium point, pushed the endpoint along the direction of the expected displacement until reaching the first target (30-mm positive displacement), gradually returned to the equilibrium point, pulled the endpoint in the opposite direction to the expected displacement until reaching the second target (30-mm negative displacement), and gradually returning to the equilibrium point. The reaction forces between the robot's endpoint and the linear actuator driving along the directions of the imposed displacement: forward–backward motion and left–right motion were recorded, as, respectively, shown in Fig. 9 and Fig. 10. The experiments were repeated for the second equilibrium point in which both joint angles were set to 30 degrees. The reaction forces recorded during the forward–backward and left–right motion are plotted against the endpoint displacement, as shown in Fig. 11 and Fig. 12.

Observed in the +Y direction about the first equilibrium point, see Fig. 9, the force magnitude increases linearly with

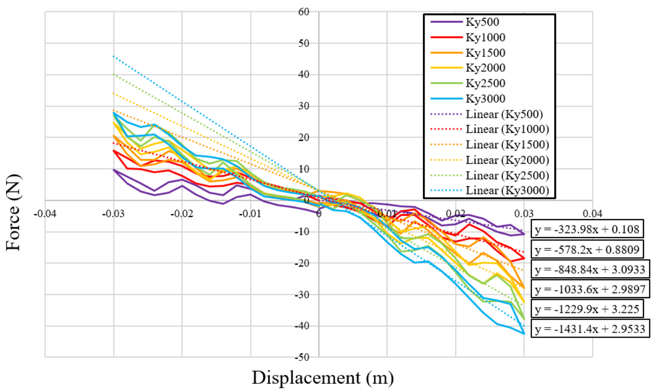

Fig. 9. Cartesian force along the forward-backward direction (Y) varies against the endpoint displacement, recorded at first equilibrium.

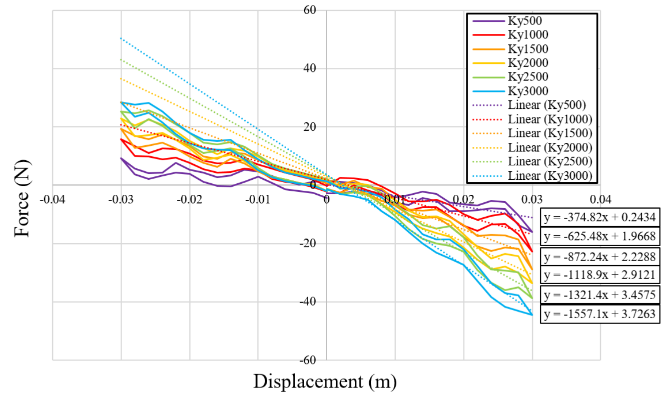

Fig. 11. Cartesian force along the forward-backward direction (Y) varies against the endpoint displacement, recorded about the second equilibrium.

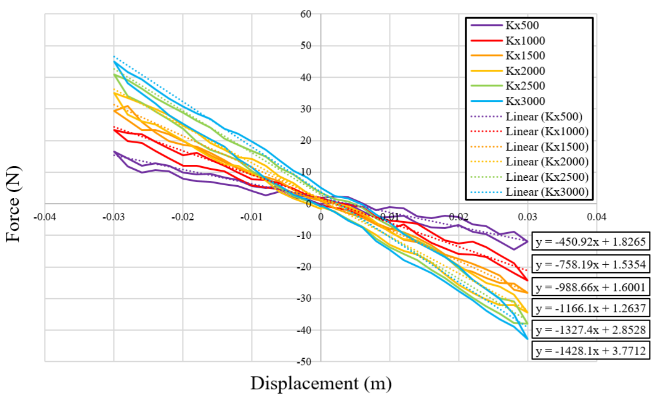

Fig. 10. Cartesian force along the left-right direction (X) varies against the endpoint displacement, recorded at first equilibrium.

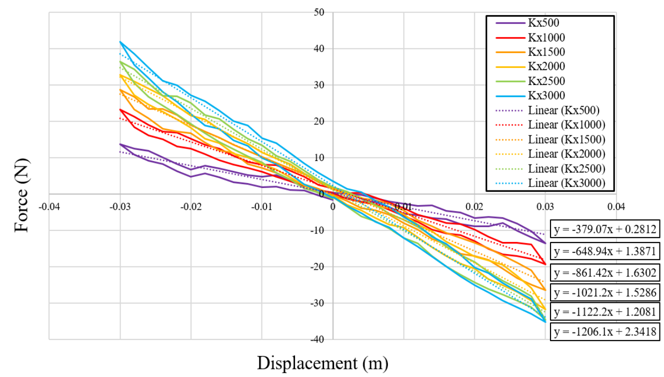

Fig. 12. Cartesian force along the left-right direction (X) varies against the endpoint displacement, recorded about the second equilibrium.

the displacement. The slope of the linear relationship increases with the desired value of Cartesian stiffness. The smaller force magnitude difference during all returning motions is related to the result of hysteresis. Although the joint stiffnesses was computed based on the expected displacement in the +Y direction, the linear relationships of a force varying against displacement are also observed from the endpoint motions in the -Y direction. However, the smaller stiffnesses (lower slope of magnitudes) can be seen obviously. The results are very similar at the second equilibrium point, see Fig. 11. A slightly higher magnitude of the force is observed at the same displacement.

In the +X direction about the first equilibrium point (see Fig. 10), the force magnitude linearly increases with the displacement. Although the slope of the linear relationship increases with the desired value of the Cartesian stiffness, the difference in slopes is less obvious at high stiffnesses. The joint stiffnesses computed based on the expected displacement in the +X direction are applicable for the −X displacement. The results are very similar at the second equilibrium point (see Fig. 12). A slightly lower magnitude of the force is observed at the same displacement.

The hysteresis effect and fluctuation in the Cartesian force along the X- and Y-axes may result from the backlash in the planetary gearbox and linear ball screw guide. Bearings, fasteners, and the flexibility of structural parts may also play significant roles in amplifying fluctuations.

B. Configuration and Directional-Dependent Stiffness Errors

For each robot arm configuration, the Cartesian stiffnesses along the Y and X directions are the slopes obtained from the linear fitting of the force varying against the endpoint displacement in the expected direction of displacement. The experimental stiffnesses in the Y direction (slopes of the plots in Figs. 9 and 11) are plotted against the designated stiffness, which is used for computing the joint stiffnesses, as shown in Fig. 13. The experimental stiffnesses in the X direction (slopes of the plots in Figs. 10 and 12) are plotted against the designated stiffness, as shown in Fig. 14.

For all configurations and directions, the stiffnesses obtained from the experiments were lower than their theoretical values. Their relationships were fitted by the quadratic functions. The nonlinear term is less significant for the stiffnesses along the Y direction (see Fig. 13). The significant nonlinear term in the X direction (see Fig. 14) may be caused by the flexibility of the robotic arm's structure. As the force increases, the structure's 3D-printed plastic absorbs more force, which could make it bend. The effect on the X direction is obvious because the motion in the X direction mainly depends on the movement of motor 2, which must pass the torque through the input link and coupler link to reach link 2.

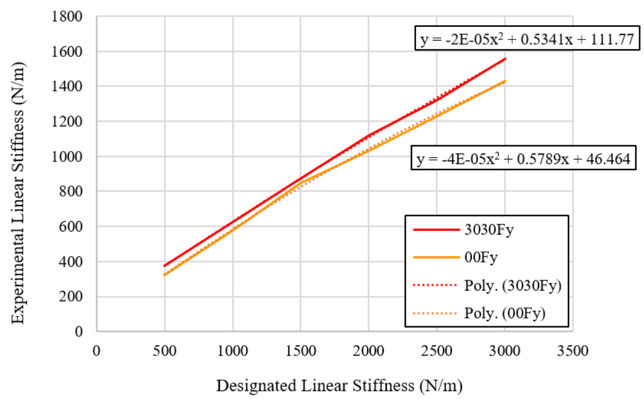

Fig. 13. Experimental stiffnesses along the Y direction (observed at two equilibrium points) are plotted against their theoretical references.

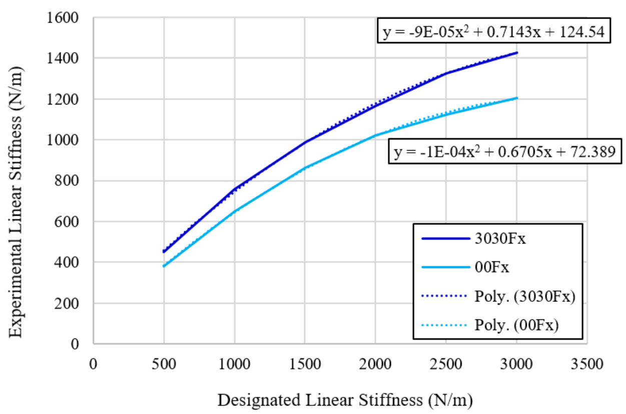

Fig. 14. Experimental stiffnesses along the X direction (observed at two equilibrium points) are plotted against their theoretical references.

VI. Conclusions

This paper presents an alternative strategy to control the Cartesian stiffness of a planar 2-DOF serial manipulator by adjusting the joint stiffnesses. The closed-form solution for mapping the stiffnesses was experimentally validated in two-direction predicted motions of the endpoint. The concept allows enhancing the performance of the stiffness control for rehabilitation robots by taking advantage of the fast joint control conveniently achieved from the affordable modular robotic actuators with integrated controllers and planetary gear reduction.

Although the linear relationships between the Cartesian force and displacement can be observed, the mappings between the experimental and designated stiffnesses are nonlinear and directional-dependent and vary against the robot arm configuration. In addition, the path direction, and joint angle displacement are required for predicting the joint stiffness. The errors and fluctuation of the force can be observed from the experiment, which could result from the structural rigidity, mechanical components, backlashes, and linear elements on the robotic arm and experimental setup.

Further studies on investigating and modeling the stiffness mapping are recommended to improve the accuracy and robustness of the control method in every direction. Finally, apart from kinematic workspace optimization, the stiffness requirement in designing the robotic arm for stiffness-controlled rehabilitation should also be considered.

Acknowledgment

This research project is partly funded by Thailand Science Research and Innovation Fund, Chulalongkorn University (IND66210017) and Tronormos Co., Ltd., Thailand.

References

[1] N. Hogan, H. I. Krebs, J. Charnnarong, P. Srikrishna, and A. Sharon, "MIT-MANUS: a workstation for manual therapy and training. I," in *Proc. IEEE Int. Works. Robot and Human Communication*, pp. 161–165, 1992.

[2] H. I. Krebs, N. Hogan, M. L. Aisen, B. T. Volpe, "Robot-aided neurorehabilitation," *IEEE Trans. Rehabil. Eng.*, vol. 6, no. 1, pp. 75–87, 1998.

[3] H. I. Krebs, et al., "Robot-aided neurorehabilitation: a robot for wrist rehabilitation," *IEEE Trans. Neural Syst. Rehabil. Eng.*, vol. 15, no. 3, pp. 327–335, 2007.

[4] H. I. Krebs, et al., "Rehabilitation robotics: performance-based progressive robot-assisted therapy," *Autonomous Robots*, vol. 15, pp. 7–20, 2003.

[5] S. H. Lee, et al., "Comparisons between end-effector and exoskeleton rehabilitation robots regarding upper extremity function among chronic stroke patients with moderate-to-severe upper limb impairment," *Sci. Rep.*, vol. 10, no. 1806, pp. 1–8, 2020.

[6] L. Zhang, S. Guo, and Q. Sun, "Development and assist-as-needed control of an end-effector upper limb rehabilitation robot," *Appl. Sci.*, vol. 10, no. 6684, pp. 1–18, 2020.

[7] L. Zollo, D. Accoto, F. Torchiani, D. Formica, and E. Guglielmelli, "Design of a planar robotic machine for neuro-rehabilitation," in *Proc. IEEE Int. Conf. Robotics and Automation*, pp. 2031–2036, 2008.

[8] J. Yamine, et al., "A planar parallel device for neuro-rehabilitation," *Robotics.*, vol. 9, no. 104, pp. 1–22, 2020.

[9] S. Nishimura, R. Chaichaowarat, and H. I. Krebs, "Human-robot interaction: controller design and stability," *in Proc. IEEE Int. Conf. Robotics and Biomechatronics*, pp. 1096–1101, 2020.

[10] R. Chaichaowarat, S. Nishimura, T. Nozaki, and H. I. Krebs, "Work in the time of Covid-19: actuators and sensors for rehabilitation robotics," *IEEJ J. Ind. Appl.*, vol. 11, no. 2, pp. 1–10, 2021.

[11] A. Javadi and R. Chaichaowarat, "Position and stiffness control of an antagonistic variable stiffness actuator with input delay using super-twisting sliding mode control," *Nonlinear Dyn.*, vol. 111, pp. 5359–5381, 2023.

[12] R. Chaichaowarat, S. Nishimura, and H. I. Krebs, "Design and modeling of a variable-stiffness spring mechanism for impedance modulation in physical human–robot interaction," in *Proc. IEEE Int. Conf. Robotics and Automation*, pp. 7052–7057, 2021.

[13] R. Chaichaowarat, S. Nishimura, and H. I. Krebs, "Macro-mini linear actuator using electrorheological-fluid brake for impedance modulation in physical human–robot interaction," *IEEE Robot. Autom. Lett.*, vol. 7, no. 2, pp. 2945–2952, 2022.

[14] F. Petit and A. Albu-Schäffer, "Cartesian impedance control for a variable stiffness robot arm," in *Proc. IEEE/RSJ Int. Conf. Intelligent Robots and Systems*, pp. 4180–4186, 2011.

[15] A. Albu-Schäffer and G. Hirzinger, "Cartesian impedance control techniques for torque controlled light-weight robots," in *Proc. IEEE Int. Conf. Robotics and Automation*, pp. 657–663, 2002.

[16] B. G. Katz, "A low cost modular actuator for dynamic robots," MS Thesis, MIT, 2018.